Solid-State Electronics 211 (2024) 108816

Contents lists available at ScienceDirect

Solid State Electronics

journal homepage: www.elsevier.com/locate/sse

Modeling the impact of incomplete conformality during atomic layer processing☆

Tobias Reiter [a,*], Luiz Felipe Aguinsky [b], Frâncio Rodrigues [b], Josef Weinbub [b], Andreas Hössinger [c], Lado Filipovic [a]

[a] Christian Doppler Laboratory for Multi-Scale Process Modeling of Semiconductor Devices and Sensors, Institute for Microelectronics, TU Wien, Wien, Austria
[b] Christian Doppler Laboratory for High Performance TCAD, Institute for Microelectronics, TU Wien, Wien, Austria
[c] Silvaco Europe Ltd., St Ives, Cambridge, United Kingdom

ARTICLE INFO

Keywords:
Atomic layer deposition
3D NAND fabrication
Thin films
High aspect ratio
Langmuir kinetics
Topography simulation

ABSTRACT

Atomic layer processing (ALP) is a modern fabrication technique for the deposition or etching of materials, which provides precise control of film thickness, composition, and conformality on a nanometer scale. This makes it crucial for the fabrication of high aspect ratio (HAR) structures, such as 3D NAND memory stacks, as its self-limiting nature provides enhanced conformality compared to traditional processes. However, as the number of NAND stacks grows and the aspect ratio continues to increase, deviations from full conformality can often occur due to precursor desorption from the surface. In this regard, a model for surface coverage during ALD in the presence of desorption, leading to incomplete conformality, has been developed and implemented in process simulation frameworks. This work is an extension of our previous research which concentrated on developing an accurate modeling approach for ALD in HAR structures (L.Aguinsky et al., *Solid State Electron.* 201, 2023). The model combines existing Knudsen diffusion and Langmuir kinetics methods and includes the Bosanquet formula for gas-phase diffusivity and reaction reversibility. It has been incorporated into academic and commercial level-set-based topography simulators. The parameters for the model have been calibrated using published results for the ALD of Al_2O_3 from trimethylaluminum (TMA) and H_2O in HAR geometries. The temperature dependence of the H_2O step is likewise analyzed, revealing an activation energy of 0.178 eV, which is consistent with recent experiments. In the TMA step, the Bosanquet formula leads to improved accuracy, and the same parameter set is able to reproduce multiple experiments, demonstrating that the model parameters accurately capture reactor conditions. Finally, the developed model is combined with atomic layer etching (ALE) to simulate the controlled, conformal deposition of HfO_2 inside HAR 3D NAND structures.

1. Introduction

The ability to accurately model incomplete conformality during semiconductor fabrication is highly important, as conformality can be a limiting factor in the design of many advanced semiconductor devices. In this manuscript, we extend on our previous work from [1], which describes incomplete conformality during atomic layer deposition (ALD), and apply the concept to a sequence of ALD and atomic layer etching (ALE) in three-dimensional (3D) NAND structures.

Recently, a particular group of thin-film processing techniques has gained significant attention, referred to as thermal Atomic Layer Processing (ALP) [2]. These techniques are characterized by the use of self-limiting reactions, that is, the surface-chemical reactions cease after all available surface sites have been saturated. This results in a high level of control over the quality and conformality of the resulting film. These self-limiting reactions can be utilized for controlled film growth in thermal ALD [3], or for precise material removal through ALE [4]. Both processes combined and used in cycles enables the possibility for area-selective deposition (ASD) in complex structures.

Partly due to the aforementioned self-limiting characteristics, ALD allows for much greater control over film thickness and conformality, when compared to conventional chemical vapor deposition (CVD) and physical vapor deposition (PVD) techniques [5]. ALD has therefore become the go-to technique in semiconductor fabrication, having found application in, e.g., thin film deposition at advanced transistor nodes, allowing for the deposition of high-k dielectric gate stacks with sub−1 nm equivalent oxide thickness (EOT) and a sub−2 nm physical

☆ The review of this paper was arranged by Sorin Cristoloveanu.

* Corresponding author.
E-mail addresses: reiter@iue.tuwien.ac.at (T. Reiter), aguinsky@iue.tuwien.ac.at (L.F. Aguinsky).

https://doi.org/10.1016/j.sse.2023.108816

Available online 2 November 2023

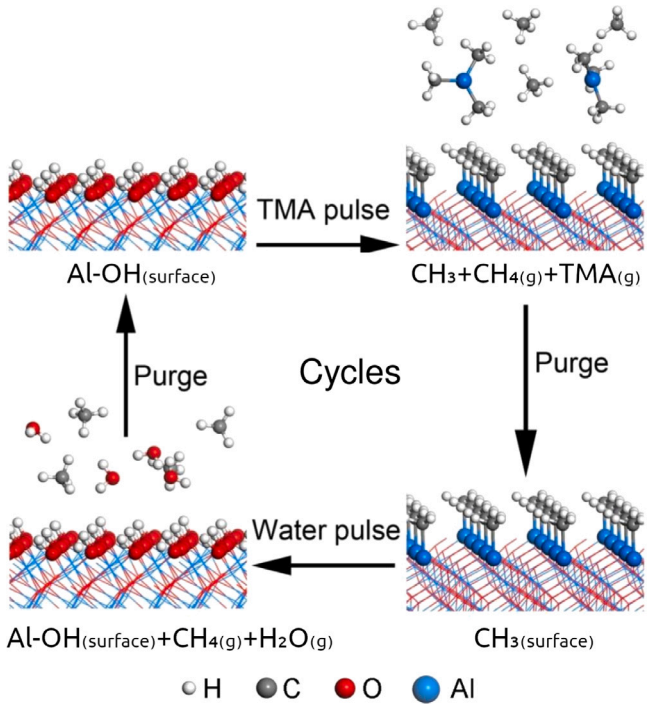

Fig. 1. Schematic illustration of the surface chemistry of Al_2O_3 ALD from TMD and water precursors. (Reprinted with permission from X.Hu [12], © The Author Xiau Hu).

thickness [6,7]. As a further benefit of its high conformality, ALD has become an important enabler in the generation of high aspect ratio (HAR) structures like dynamic random-access memory capacitors [8] and 3D integration of novel memory devices such as 3D NAND or future 3D DRAM [9].

ALD differs from traditional CVD by dividing the chemical reaction to initiate growth into at least two sequential cycles of self-limiting steps [7]. One of the best-known examples of thermal ALD is the deposition of aluminum oxide (Al_2O_3) from trimethylaluminum (TMA) and water, as shown in Fig. 1 [10], which is a commonly used process in the production of high-k capacitor films for DRAM [8]. The reason for its popularity is due to the near-ideal surface chemistry involved. As a result, extensive research has been conducted on this process, making it the benchmark for evaluating new ALD methods. Notably, increased research attention has been placed on this process after the development of a lateral HAR structure tailored towards film conformality analyses [11]. Due to the vast amount of research dedicated, ALD of Al_2O_3 using TMA/water precursors is typically used to calibrate models such as the one presented in this study.

Assuming fully self-limiting reactions with unchanging reactor conditions, perfect conformality is theoretically achievable by adjusting the step pulse time t_p to the HAR structure. In principle, the film thickness can be easily controlled by adjusting the growth per cycle (GPC) parameter, which is determined by the reactants and reactor conditions, and the total number of cycles N_{cycles}. However, in real-world situations, deviations from complete conformality in HAR structures often occur due to imperfect self-limiting surface chemistry and limited reactant transport [5].

As semiconductor technology advances, requiring ever more extreme HAR features [13], the challenge of understanding incomplete conformality in ALD must be addressed from a combined experimental and modeling approach. A recent review paper from Cremers et al. summarizes the research effort on this question [5]. Significant experimental strides have been made after the development of a lateral HAR structure tailored to film conformality analyses [11]. In modeling aspects, the majority of the proposed approaches relies on simplifying the complex and not fully understood surface chemistry [14] to a first-order Langmuir model [5]. First-order Langmuir models have been developed and utilized to predict saturation times [15–17], model growth kinetics [18], determine scaling laws [19], and to calculate the clean surface sticking coefficient (β_0) through either Monte Carlo methods [20,21] or simplified analytical expressions [22]. While these methods are highly effective, they do not provide thickness profiles which can be easily integrated with process simulators, specifically those employing implicit surface representations, such as level-set topography simulators. This compatibility is necessary for incorporating ALD models into process simulations and for design-technology co-optimization (DTCO) workflows for device and circuit simulation [23].

In previous studies, we were able to examine the ALD of titanium compounds in a level-set-based topography simulator through a time-discretization of each ALD cycle. These include detailed Langmuir surface adsorption models with Monte Carlo ray tracing calculations of local reactant fluxes [24]. While this is useful in studying the surface conditions on complex geometries during one or a few ALD steps, the approach is too slow when examining tens or hundreds of ALD steps in succession. To enable a topography model for realistic ALD processes which involve hundreds of cycles, the surface coverages and velocities must be tracked over long fabrication times. This means that time discretization of single ALD steps renders the simulation computationally unfeasible.

In this manuscript we present an extension of the model we presented in [1] which is based on one-dimensional (1D) diffusive particle transport, building upon the models of Yanguas-Gil and Elam [17] by combining it with physical–chemical phenomena highlighted in previous works [15,18,25]. The model includes reversible reactions and gas-phase diffusion through the Bosanquet formula [26] and the calculation of thickness profiles is efficiently integrated with several level-set based topography simulators [27–30] through the bundling of multiple cycles via the introduction of an artificial time unit. While the initial model was calibrated to reported ALD thicknesses of Al_2O_3 in both the H_2O- and TMA-limited regimes, in this study, we extend the model towards the fabrication of 3D NAND-like structures and the deposition or etching of hafnium dioxide (HfO_2) in HAR 3D NAND stacks. After calibrating the model to experimental conditions by adjusting the evaporation flux and sticking coefficient, we present a simulation of a structure with an aspect ratio of approximately 50, showing an obvious variation in film thickness between the top and bottom of the structures, induced by the non-idealities in conformality.

2. Simulation methods

Modeling and simulations of ALP, and especially ALD, is being investigated at many length and time scales [12,31–33]. At the atomistic scale, it is quite common to apply *ab-initio* approaches, such as density functional theory (DFT) to understand how the precursor molecules bind to the surface and to examine the structural and electronic properties of precursors at the lowest scales [34]. Computational fluid dynamics (CFD) using continuum models are often applied in order to understand how precursors behave at the macro scale and how the ambient equipment settings impact the gas distribution inside the ALD reactor [35]. In this manuscript we model ALD at the mesoscale as our main purpose is to provide a description of the changing topography during ALD and the integration of this model in a broadly applicable process simulation framework. This typically requires the assumption of ballistic transport in the chamber to calculate the precursor flux at the surface, where Langmuir adsorption models are applied to describe the interaction between the precursors and the substrate surface [1,24].

2.1. Surface kinetics

The typical means to model the impact of ALD on the evolving topography is to assume that the surface processes are limited by the reactive transport of one of the precursors [5]. In this study, to present a generic ALD model, we concentrate on the water-limited regime during ALD of Al_2O_3, while the same insights can be applied to generate a model for the TMA-limited case or to other reactants. A first-order Langmuir surface kinetics model is combined with diffusive reactant transport in order to calculate surface coverage θ. This model is an enhancement on the original model proposed by Yanguas-Gil and Elam [17], with the aim of taking into account reversible kinetics and the effect of gas-phase diffusivity [15,18,25].

Prior to the release of water into the ALD reactor, the surface is assumed to be fully covered by CH_3 terminations, which are connected by an Al atom to the Al_2O_3 substrate, as can be visualized in Fig. 2. The following processes are observed therein as a consequence of an impinging flux of water molecules Γ_{H_2O} ($m^{-2}\ s^{-1}$) reaching the substrate surface:

(a) Adsorption: As a water molecule impinges on the surface, it may react with the exposed surface-adsorbed CH_3. This would cause a chemical reaction by which H_2O splits into OH^- and H^+, whereby the H^+ binds with the adsorbed CH_3, forming CH_4 and releasing it from the surface. The substrate surface then becomes OH-terminated. The probability of this taking place is understood as the H_2O sticking probability $\beta(\theta)$, which is dependent on the current surface coverage of OH θ. Effectively, what this means is that this reaction can only occur at surface locations where the CH_3 is still exposed, i.e., where such a reaction has not already taken place. Therefore, assuming that a physical probability for the reaction between H_2O and CH_3 is given by β_0, the sticking probability for the surface, which depends on the current coverage, is then given by $\beta(\theta) = \beta_0(1-\theta)$.

(b) Reflection: As a water molecule approaches the surface, if it approaches a region where no CH_3 is exposed and the adsorption reaction cannot take place, a diffuse reflection will occur, whereby the H_2O molecule is reflected away from the surface, free to interact with another surface site. The probability of a reflection taking place is the opposite to the probability of adsorption and is, therefore, described by $1 - \beta(\theta)$.

(c) Desorption: Since thermal ALD requires heating the substrate to temperatures in the range of 150 °C to 300 °C, some evaporation of surface-adsorbed OH molecules can take place, resulting in the desorption of this molecule and a reduction in the uniform coverage on the surface. The desorption is given by the evaporation flux Γ_{ev} ($m^{-2}\ s^{-1}$). This effect is primarily ignored in the original model and in many subsequent developments which assume irreversible kinetics (i.e., $\Gamma_{ev} = 0$) [17,19,36,37].

Nevertheless, several studies have looked into the impact of evaporation on the surface coverages and noted the importance of including this in models, especially for HAR structures, leading to the following first-order representation of the time evolution of the surface coverage of OH θ at each surface point given by $\vec{r}$

$$\frac{1}{s_0}\frac{d\theta(\vec{r})}{dt} = \Gamma_{H_2O}(\vec{r})\overbrace{\beta_0\left(1-\theta(\vec{r})\right)}^{\beta(\theta)} - \Gamma_{ev}\theta(\vec{r}), \tag{1}$$

where s_0 (m^2) is the surface site area, which is commonly estimated with a "billiard ball" approximation from the deposited film density ρ ($kg\ m^{-3}$) and growth per cycle GPC (Å) [18]. The above Eq. (1) describes an empirical model using two phenomenological parameters, mainly the sticking coefficient of H_2O with surface-absorbed CH_3, β_0, and the evaporation flux, Γ_{ev}. In order to be able to apply this surface model, the coverage $\theta(\vec{r})$ of the relevant precursor has to be calculated, which depends on the flux distribution along the substrate surface $\Gamma_{H_2O}(\vec{r})$.

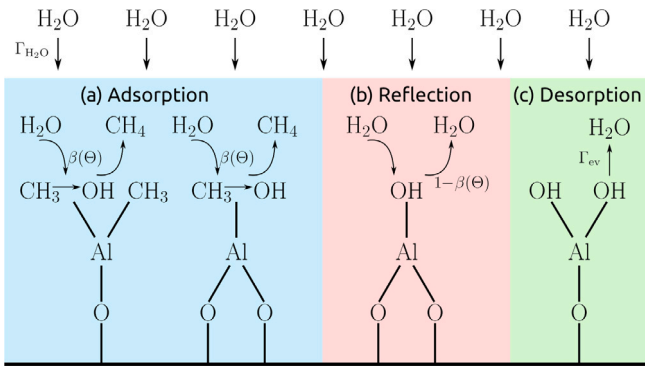

Fig. 2. Possible reaction pathways in reversible Langmuir kinetics for the H_2O step of ALD of Al_2O_3. (Reprinted from Aguinsky et al. *Solid State Electron.* 201, 108584 (2023) [1], © The Authors, licensed under the CC BY 4.0 License, https://creativecommons.org/licenses/by/4.0).

2.2. Flux determination

The calculation of $\theta(\vec{r})$ requires determining the distribution of the reactant flux $\Gamma_{H_2O}(\vec{r})$, which can be difficult as $\beta(\theta)$ changes across the surface and after each step of solving (1). While methods such as the Boltzmann transport equation [15], the lattice Boltzmann model [38], or Monte Carlo ray tracing [20,24] can provide accurate results, they are computationally intensive, making them unfeasible to study several hundreds ALD cycles in succession. To simplify the calculation, we make the assumption that the flux is equal on all surfaces at the same z coordinate, allowing us to use the continuity equation and a 1D differential equation to describe diffusive flow in a cylinder of diameter d and length L with adsorption losses [17,39],

$$\begin{aligned} D\frac{d^2\Gamma_{H_2O}(z)}{dz^2} &= \frac{\bar{v}}{d}\beta_0\left(1-\theta(z)\right)\Gamma_{H_2O}(z), \\ \Gamma_{H_2O}(0) &= \Gamma_0, \\ D\frac{d\Gamma_{H_2O}}{dz}\Big|_{z=L} &= -\frac{1}{4}\bar{v}\beta_0\left(1-\theta(L)\right)\Gamma_{H_2O}(L), \end{aligned} \tag{2}$$

where $\bar{v}$ ($m\ s^{-1}$) is the thermal speed and Γ_0 ($m^{-2}\ s^{-1}$) is the flux of the reactant species inside the reactor, which can be calculated using the kinetic theory of gases [40] from the reactor temperature T (°C), reactant molar mass M_A ($kg\ mol^{-1}$), and partial pressure p_A (mTorr). Particle transport is assumed to be at equilibrium, since the particle speed is several orders of magnitude faster than the chemical evolution of the surface [17,39].

The system of equations given by (1) and (2) is a reiteration of the Yanguas-Gil and Elam model [17] with extensions to consider reversibility in the surface reaction and an explicit representation of the diffusivity D ($m^2\ s^{-1}$). This allows to combine the model with Knudsen diffusion through the Bosanquet interpolation formula, discussed in more detail in [1]. These physical–chemical phenomena have been incorporated in previous studies [15,18,21,25]; however, such models, most notably the approach taken by Ylilammi et al. [18] and its subsequent expansion [25], rely on a different set of approximations for the calculation of the flux distribution inside the structure and do not compute a solution to (2).

In essence, the diffusion D is made up of two separate components: One resulting from collisions between the reactant and the wall (Knudsen diffusivity D_{Kn}), and another from collisions between reactants (gas-phase diffusivity D_A). Historically, the concept of Knudsen diffusion has been associated with a long cylindrical tube of diameter d [41], yielding the following expression for diffusivity [26]:

$$D_{Kn} = \frac{1}{3}\bar{v}d \tag{3}$$

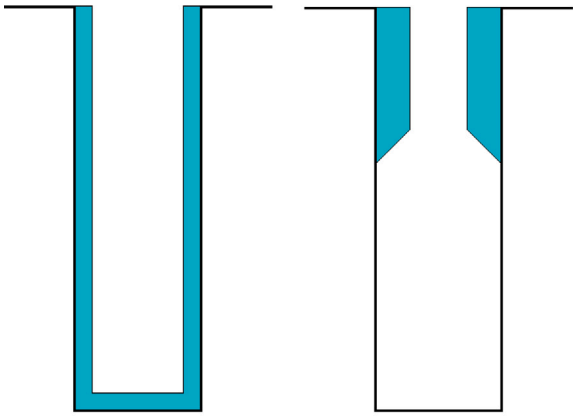

Fig. 3. Schematic representation of thickness profiles for (a) reaction-limited and (b) diffusion limited ALD processes.

When a structure other than a long cylinder is considered, a mapping between the desired geometry and the cylinder must be introduced. For our study, the hydraulic diameter approximation is employed [18], wherein the diameter d in (2) and (3) is replaced by $d \rightarrow h_d \cdot d$, where h_d is the hydraulic diameter factor and d is a relevant physical dimension. For example, for a wide rectangular trench with opening d, h_d is estimated to be equal to 2 [5,18]. If the frequency of inter-particle collisions is comparable to the frequency of particle–wall collisions, then the Bosanquet interpolation formula is applied [26]

$$\frac{1}{D} \approx \frac{1}{D_A} + \frac{1}{D_{\mathrm{Kn}}}, \tag{4}$$

where D_A is the conventional Chapman-Enskog gas-phase diffusivity [40] calculated from the particle hard-sphere diameter d_A (pm). Otherwise, if the particle–wall interactions dominate and the Knudsen number is quite large (i.e., $\mathrm{Kn} > 10$), then assuming Knudsen diffusion alone and solving (3) is sufficient. In this work Knudsen diffusivity ($D_A \rightarrow \infty$) is assumed, except when explicitly indicated otherwise.

Typically, the precursor diffusion through a HAR geometry can have significant implications on the deposited profiles after ALD [42]. When diffusion has no impact, the coverage is said to be reaction-limited, resulting in a highly conformal deposition, as noted in Fig. 3(a). Diffusion-limited regimes show the most non-conformality, shown in Fig. 3(b), since blocking the precursor from reaching the depths of the trench effectively impedes the surface reaction from taking place.

2.3. Topography simulation

To determine the change in the thickness profiles during ALD fabrication in a way which allows for the simulation of subsequent processing steps, meshing and application of structures in device simulators for a complete DTCO sequence, it is important to describe the interfaces and surfaces accordingly. Level-set based methods are a way to achieve this. This method uses a signed distance function (SDF) $\Phi(\vec{x})$ represented on a grid, whereby each point on the grid $\vec{x}$ stores its distance to the surface, meaning that the surface is not explicitly stored [27,28]. This method of implicitly defining the surfaces is applied in commercial process simulators, such as Silvaco's *Victory Process* [30] as well as in our in-house process simulator ViennaPS [43] which uses the in-house developed level-set library ViennaLS [29] to store the geometry under investigation.

With the level-set method, the surface is defined to be at locations where the SDF is equal to a specific scalar value, typically zero. The surface is, therefore, said to be the zero level-set. The SDF $\Phi(\vec{x})$ is constructed based on the signed distance d of a domain point $\vec{x}$ from the surface S bounding the volume M:

$$\Phi(\vec{x}) = \begin{cases} -d, & \vec{x} \in M \\ 0, & \vec{x} \in S \\ d, & \vec{x} \notin M \end{cases} \tag{5}$$

The time evolution of a surface represented by $\Phi(\vec{x})$ is described by the surface normal velocity $v(\vec{x})$. For a typical geometry with non constant SDF gradients, the gradient is used to normalize $v(\vec{x})$, which leads to the level set equation:

$$\frac{\partial \Phi(\vec{x},t)}{\partial t} + v(\vec{x}) \left| \nabla \phi(\vec{x},t) \right| = 0 \tag{6}$$

Since (6) is a form of the Hamilton–Jacobi equations, many algorithms exist which can be used to solve it with various finite difference schemes [44,45] and using parallelization algorithms [46]. With (6), the velocity is used to update the values of $\phi(\vec{x})$ in time. As the surface evolves, the points remain at the same position while their SDF changes [28]. It should also be noted that the velocity needs to be defined on all grid points $v(\vec{x})$, while the model will only give surface velocities at surface locations $v(\vec{r})$ (typically requiring velocity extension algorithms [47]). In essence, the velocity field is populated by assigning the velocity at each grid point $\vec{x}$ to be equal to the velocity calculated at the nearest surface point $\vec{r}$.

The main requirement of our growth model is to identify the velocities along the surface of our geometry of interest, which is derived from a calculation of the arriving fluxes Γ and coverages θ, discussed in the previous sections. However, mapping $\theta(\vec{r})$ into $v(\vec{r})$ is not straightforward. We should also consider that the time t in (6) is physical, while we need to discretize time as it relates to growth-per-cycle (GPC). In previous studies, we have calculated the growth rates cycle-by-cycle by evolving the surface by the molecular layer thickness [24]; however, this imposes a performance penalty since the grid resolution and time steps must be small enough to capture the individual molecular layer and $\theta(\vec{r})$ must be calculated N_{cycles} times - once for each cycle. This calculation repeats even though the geometry changes minimally between sequential cycles, making it useful for studying a few cycles, but not when tens or hundreds of cycles should be modeled.

To accurately simulate an ALD process with a large number of cycles, a more efficient approach is necessary. We achieve this by grouping multiple cycles into a single surface evolution step. This is achieved by introducing an artificial time $t^* = N_{\mathrm{cycles}}/C$, where C is a numerical constant. It is important to note that t^* is not related to t_p which is only used to calculate $\theta(\vec{r})$. Essentially, t^* represents a bundle of multiple ALD cycles, maintaining consistency with (6), and the velocity field becomes

$$v(\vec{r}) = v(z) = C \cdot \mathrm{GPC} \cdot \theta(z). \tag{7}$$

The value of the constant parameter C can be set by considering the number of cycles required such that $t^* \approx 1$. In level-set based topography simulators, $v(\vec{r})$ is assumed to be constant during each solution during a time step Δt of (6), subject to the Courant–Friedrichs–Lewy (CFL) condition, which restricts the time step to not exceed one grid spacing during a single time step, i.e., $\Delta t < \Delta x / \max \left| v(\vec{r}) \right|$ [27]. After each time step, the input parameters d and L in (2) are updated. Therefore, for Eq. (7) to be accurate, Δx must be small enough to avoid significant changes in the geometry affecting $\theta(\vec{r})$.

3. Model calibration

As mentioned previously, the most well-studied ALD process is the deposition of Al_2O_3 from TMA and H_2O precursors. Therefore, this is also the starting point to our modeling and simulation approach in order to ensure that the proposed modeling sequence, described in Section 2, is properly devised and implemented. The developed workflow will subsequently also be used to calibrate a model for the atomic layer

Table 1
Calibrated model parameters for the H_2O step of ALD of Al_2O_3. The measured values are taken from [22].

Parameter	150 °C	220 °C	310 °C
Γ_{ev} (m^{-2} s^{-1})	$6.5 \cdot 10^{19}$	$5.0 \cdot 10^{19}$	$3.5 \cdot 10^{19}$
β_0	$5.0 \cdot 10^{-5}$	$1.2 \cdot 10^{-4}$	$1.9 \cdot 10^{-4}$
β_0, estimate from [22]	$1.4 \cdot 10^{-5}$ – $2.3 \cdot 10^{-5}$	$0.8 \cdot 10^{-4}$ – $2.0 \cdot 10^{-4}$	$0.9 \cdot 10^{-4}$ – $2.5 \cdot 10^{-4}$

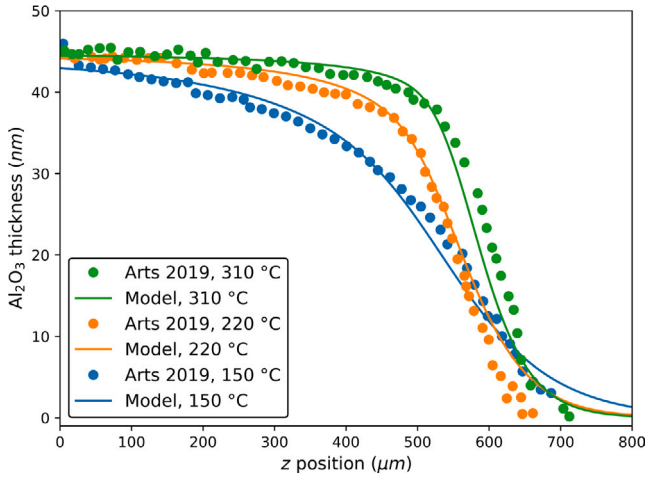

Fig. 4. Comparison of topography simulation using the combined surface coverage model with the parameters from Table 1 to H_2O-limited thickness profiles measured by Arts et al. [22]. (Reprinted from Aguinsky et al. *Solid State Electron.* 201, 108584 (2023) [1], © The Authors, licensed under the CC BY 4.0 License, https://creativecommons.org/licenses/by/4.0).

deposition of HfO_2 from tetrakis(ethylmethylamino)hafnium (TEMAH) and water precursors in high aspect ratio 3D NAND trenches as well as the atomic layer etching (ALE) of the HfO_2 layer using dimethylaluminum chloride (DMAC) and HF [9,48–50].

3.1. ALD of Al_2O_3: The H_2O step

In this section, the model workflow described in Section 2 is calibrated to the measured thickness profiles of Al_2O_3 in the H_2O-limited regime. Arts et al. [22] studied the film thickness in lateral HAR trench-like structures, with dimensions $d = 0.5$ μm, $L = 5000$ μm, after 400 ALD cycles with a GPC of 1.12 Å and an H_2O dose of 750 mTorr s at three calibrated substrate temperatures T: 150 °C, 220 °C, and 310 °C. The values of $t_p = 0.1$ s and $s_0 = 3.36 \cdot 10^{-19}$ m^2 were estimated for this process in our previous work from visual inspection and manual calibration to the experimental data [1]. The results are shown in Table 1 and the comparison to the experimental data is illustrated in Fig. 4. The authors in [22] also calculated β_0 from the slope at 50% height and those values are likewise reported in Table 1.

In Fig. 4, a good match between the experimental profiles and our simulated topographies, using the combined model for surface coverage, is observed. The estimated values for β_0 are also in line with the estimated ranges from the original study, which is expected since the original study also uses first-order Langmuir kinetics. Our methodology is nevertheless believed to provide a more precise estimate for β_0, including for the discrepant value at 150 °C, as we take into account the entire profile and include the evaporation flux Γ_{ev}. However, it is nevertheless possible that we underestimate the impact of Γ_{ev} as we do not factor in the time required for the purge step. The decreased thickness and smoother transition between the high growth region for that profile strongly suggests the impact of reversible reactions, which is supported by other modeling studies [25].

Table 2
Model parameters for the TMA step of ALD of Al_2O_3 calibrated to multiple measurements from [18,22,51].

Parameter	300 °C
Γ_{ev} (m^{-2} s^{-1})	$3.0 \cdot 10^{19}$
β_0	$7.5 \cdot 10^{-3}$
β_0 from [18]	$5.7 \cdot 10^{-3}$
β_0 from [22][a]	$(0.5 - 2.0) \cdot 10^{-3}$
β_0 from [51]	$4.0 \cdot 10^{-3}$

[a] Temperature of experiment was 275 °C.

From the available experimental values, we were able to fit Arrhenius relationships for the two model parameters (β_0 and Γ_{ev}), which allows to estimate the behavior of this ALD process for a wider set of process temperatures T. We observe that the sticking probability β_0 reduces with increasing temperature, while the evaporation flux Γ_{ev} is increased along the following fitted expressions

$$\beta_0 = 6.993 \times 10^{-3} \cdot \exp\left(\frac{-0.178}{k_B T}\right)$$
$$\Gamma_{ev} = 7.246 \times 10^{18} \cdot \exp\left(\frac{0.082}{k_B T}\right), \quad (8)$$

where k_B is the Boltzmann constant and the values have coefficients of determination of 0.975 and 0.924, respectively.

3.2. ALD of Al_2O_3: The TMA step

The above-described model has also been manually calibrated to the published thickness profiles of ALD-deposited Al_2O_3 in the TMA-limited regime in the same way as was described in Section 3.1. Given the higher complexity of TMA, more research has been conducted in this area, enabling us to use our model on multiple independent experiments in similar lateral HAR structures with a width of $d = 0.5, \mu m$, [18,22,51]. All available information on the reactor and film parameters was obtained directly from the original publications.

Since all thickness profiles were recorded at a limited range of temperatures (275 °C in [22] and 300 °C otherwise), the model is manually calibrated to all profiles using the parameter set provided in Table 2. This table also includes the estimated values of β_0 from the original studies; the differences observed in the results are likely due to the impact of Γ_{ev}, which is ignored in the other studies, with the exception of [18]. A comparison between our model and the published experimental profiles is given in Fig. 5, where a good agreement is demonstrated. It should be noted that the peaks observed in the experimental data at the z position between 150 μm and 200 μm from [51] were disregarded as they were reported to be due to spurious interactions with the pillars supporting the lateral structure. It is likely that these pillars are also the principal cause for the discrepancy in the thickness values in their immediate vicinity.

In Fig. 6 we apply our model in order to reproduce the experiments from Yim and Ylivaara et al. for lateral HAR structures with varying initial opening widths d [51]. We observe an excellent match to the experimental results, with a slight deviation in the model when $d = 2.0$ μm, which is a result of the assumption of pure Knudsen diffusivity, which is no longer valid since $Kn \approx 8.9$ for this test case. When we apply the Bosanquet method from (4), which calculates the hard-sphere diameters of TMA ($d_{TMA} = 591$ pm) and of the carrier gas N_2 ($d_{N_2} = 374$ pm) [18], the accuracy is significantly improved.

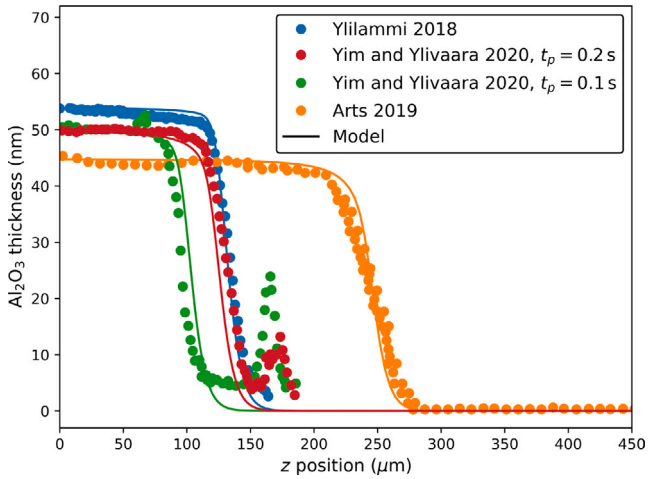

Fig. 5. Comparison of our models with parameters from Table 2 to TMA-limited thickness profiles from Ylilammi et al. [18], Arts et al. [22], and Yim and Ylivaara et al. [51]. (Reprinted from Aguinsky et al. *Solid State Electron.* 201, 108584 (2023) [1], © The Authors, licensed under the CC BY 4.0 License, https://creativecommons.org/licenses/by/4.0).

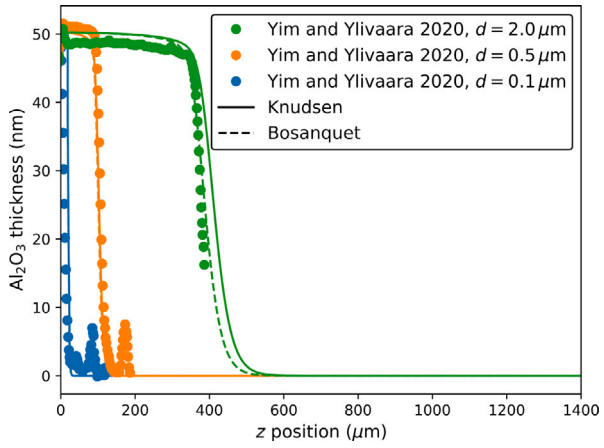

Fig. 6. Comparison of simulated structures to profiles reported by Yim and Ylivaara et al. [51] for lateral HAR structures with different initial openings d using parameters from Table 2. "Knudsen" shows the model using only Knudsen diffusivity, while "Bosanquet" includes gas-phase diffusivity. (Reprinted from Aguinsky et al. *Solid State Electron.* 201, 108584 (2023) [1], © The Authors, licensed under the CC BY 4.0 License, https://creativecommons.org/licenses/by/4.0).

4. ALP in 3D NAND structures

The ongoing development of thermal ALP technology can unlock the potential for the 3D integration of novel memories. As evidenced by the success of 3D NAND flash memory, it is possible to create a vertical 3D stack of charge storage structures without relying on planar technology. This stacking method has significantly increased the density of memory technology, making it applicable to other novel memory technologies such as resistive random-access memory (ReRAM). However, achieving conformality in thermal ALP is crucial for the patterning of these material stacks on the sidewalls of a HAR structure. Topography modeling can provide valuable insight into the reactive transport issues which limit conformality and facilitate the investigation and simulation of devices with realistic shapes.

Fischer et al. from Lam Research have created a 3D NAND-like testing framework to explore thermal ALD and ALE techniques, in order to assist in the development of novel 3D memory technologies [9]. They composed a structure of either 76 or 98 stacked oxide-nitride

Table 3
Calibrated model parameters for ALD of HfO_2 for the hafnium step to experimental data from Fischer et al. [9].

Γ_{ev} (m^{-2} s^{-1})	β_0
$3.5 \cdot 10^{22}$	$7.0 \cdot 10^{-3}$

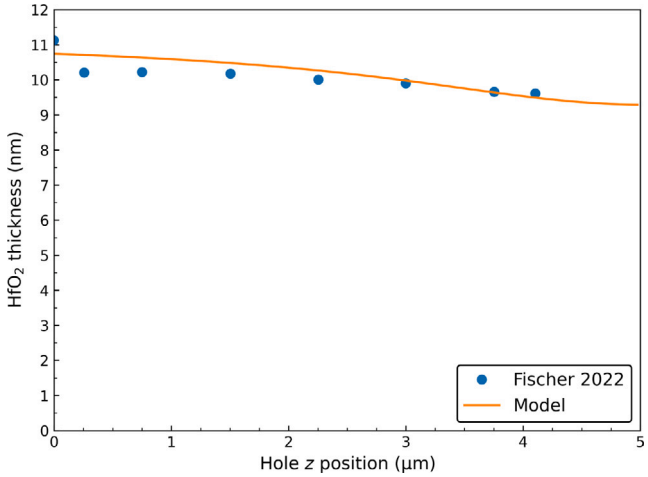

Fig. 7. Comparison of simulated topography using parameters from Table 3 to ALD of HfO_2 in a 3D NAND-like test structure reported by Fischer et al. [9].

(ON) layers to a maximum height of 4 μm or 5 μm, respectively. In this stack, a cylindrical hole is etched using a high-energy reactive ion etching (RIE) technique. After performing the ALP, the whole structure is cleaved and imaged with transmission electron microscopy (TEM). On the basis of this test structure, Fischer et al. [9] demonstrate ALD of HfO_2 achieving a step coverage of 85% while additionally investigating a subsequent ALE process under different reactor conditions.

In order to compare the presented model to the experimental results by Fischer et al. the parameters have to be first calibrated accordingly. We then apply the calibrated model to the 3D NAND test structure and compare the results.

4.1. ALD of HfO_2

The thermal ALD process in the 3D NAND structure by Fischer et al. [9] uses H_2O and an undisclosed hafnium-based reactant (most likely $HfCl_4$ [48] or TEMAH [16]) for the deposition of HfO_2. In order to simulate to reported thickness profile, the hafnium reactant TEMAH is assumed to be the limiting species, with the relevant parameters extracted from [16], although providing a variation with a model using $HfCl_4$ would be trivial. From this, the calibrated evaporation flux and sticking coefficient can be found in Table 3. Silvaco's process simulation framework Victory Process [30] is used to simulate the entire 3D NAND-like stack proposed in [9]. The ON deposition and the RIE hole etching step are assumed to be ideal and are thus geometrically modeled. The presented reactive transport model for thermal ALP is implemented in Victory Process' Open Model Library and applied to simulate the HfO_2 ALD step. In Fig. 7, the resulting deposition thickness is compared to the experimental data.

4.2. ALE of HfO_2

As shown by Murdzek et al. thermal ALE conventionally follows fluorination and ligand-exchange processes with self-limiting characteristics, similar to thermal ALD [49]. We can therefore use the presented model also for simulating an ALE process by calibrating the parameters

Table 4
Calibrated model parameters for DMAC-limited ALE of HfO_2 to experimental data from Fischer et al. [9].

Reactor condition	Γ_{ev} (m^{-2} s^{-1})	β_0	s_0 (m^{-2})
Low pressure, 250 °C	$2.5 \cdot 10^{17}$	$6.0 \cdot 10^{-4}$	$7.0 \cdot 10^{-21}$
High pressure, 350 °C	$1.0 \cdot 10^{18}$	$5.0 \cdot 10^{-3}$	

to experimental results. Fischer et al. propose thermal ALE of HfO_2 from dimethylaluminum chloride (DMAC) and HF [9]. They explore both low-pressure and high-pressure reactors in-depth in order to fully understand the required DMAC dosage. In order to evaluate various reactor settings, an etch amount per cycle (EPC) profile was extracted from each experimental TEM observations.

With a process pressure of 30 mTorr for both the DMAC and HF steps, the low-pressure reactor experiments were carried out at 250 °C with no background gas. By adjusting the pulse duration, two HF dose configurations – a low dose of 5 s and a high dose of 30 s – were studied. The DMAC dose was adjusted by varying the pulse duration from 5 s to 90 s.

The high-pressure tests used N_2 as a carrier gas for etching at 350 °C with a total process pressure of 1 Torr. Since the DMAC partial pressure was held constant at 48 mTorr, the dose was adjusted by varying the pulse duration from 3 s to 90 s. Additionally, there were two sets of studies with different HF doses. The low HF dose was attained using a partial pressure of 150 mTorr for a pulse time of 2 s. For 60 s, the high HF dose had a partial pressure of 400 mTorr. The authors of the original study noted that EPC declines with comparably lower DMAC doses. They conclude that a very large dose is required to enable thermal ALE.

It has also been reported that the HF dose only has a very slight impact on the EPC profile [9]. Therefore, we can reasonably apply the presented model under the assumption that the DMAC is the limiting reactant. Due to the complex fluorination and ligand-exchange chemical process, the "billiard ball" approximation cannot be used to calculate s_0. It is instead treated as an additional model parameter. The transport in the high-pressure reactor is clearly not in the molecular flow regime and thus the Bosanquet interpolation formula is applied with $d_{N_2} = 374$ pm and the DMAC radius is estimated from its liquid density to be $d_{DMAC} = 748$ pm. The simulated EPC profiles, which are shown in Fig. 8 in comparison to experimental data from Fischer et al. [9], are obtained by dividing the etch depth at each z position by $N_{cycles} = 20$. Table 4 contains the calibrated parameters, including s_0.

The calibrated simulations in Fig. 8 show only a qualitative agreement, since the TEM data has comparatively higher noise than the optical profilometry reported in Section 3. Nevertheless, the calibrated parameters enable the first estimations of β_0 for DMAC which has not been reported to date. Furthermore, the increase in β_0 with temperature is a sign of Arrhenius-like behavior, comparable to that shown in Eq. (8). Contrary to the analysis in Section 3.1, the evaporation flux also seems to increase with temperature. This unexpected behavior should be investigated in further studies.

The entire 3D NAND-like stack after sequential ALD and ALE can be seen in Fig. 9. The non-ideality of the simulated process can be observed in the varying HfO_2 film thickness between the top, middle and bottom regions of the stack. This shows good qualitative agreement with the experimental results by Fischer et al. shown in Fig. 10. Although the test structure itself is not a physically operable device, this simulation workflow shows a path for seamless DTCO workflow integration.

5. Conclusion

Our work introduces a novel model to address incomplete conformality during atomic layer deposition (ALD) in high aspect ratio (HAR) structures. The model is based on the combination of diffusive particle

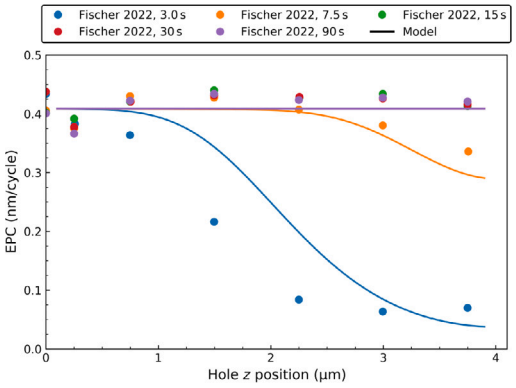

(a) High pressure, high HF dose

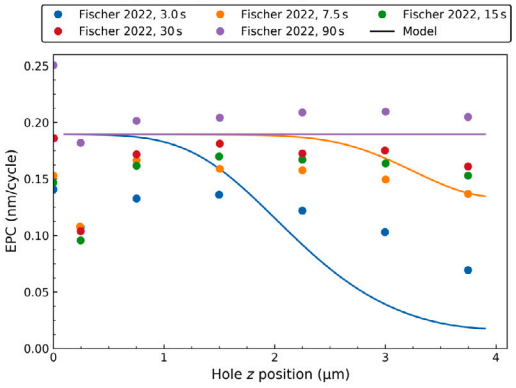

(b) High pressure, low HF dose

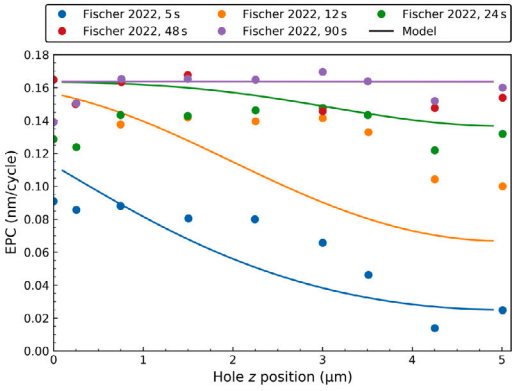

(c) Low pressure, high HF dose

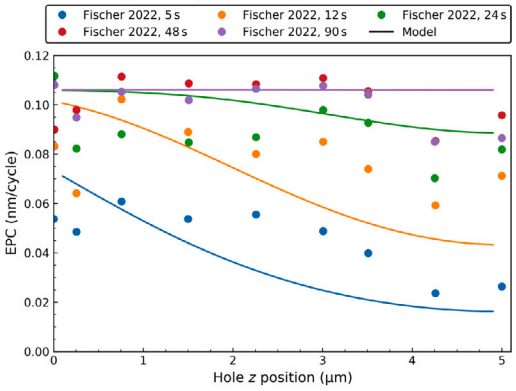

(d) Low pressure, low HF dose

Fig. 8. Comparison of simulated ALE using parameters from Table 4 to DMAC-limited ALE of HfO_2 in a 3D NAND-like test structure reported by Fischer et al. [9]. Both a low-pressure (30 mTorr) and a high-pressure (1 mTorr) reactor conditions are simulated, including different doses of HF and DMAC.

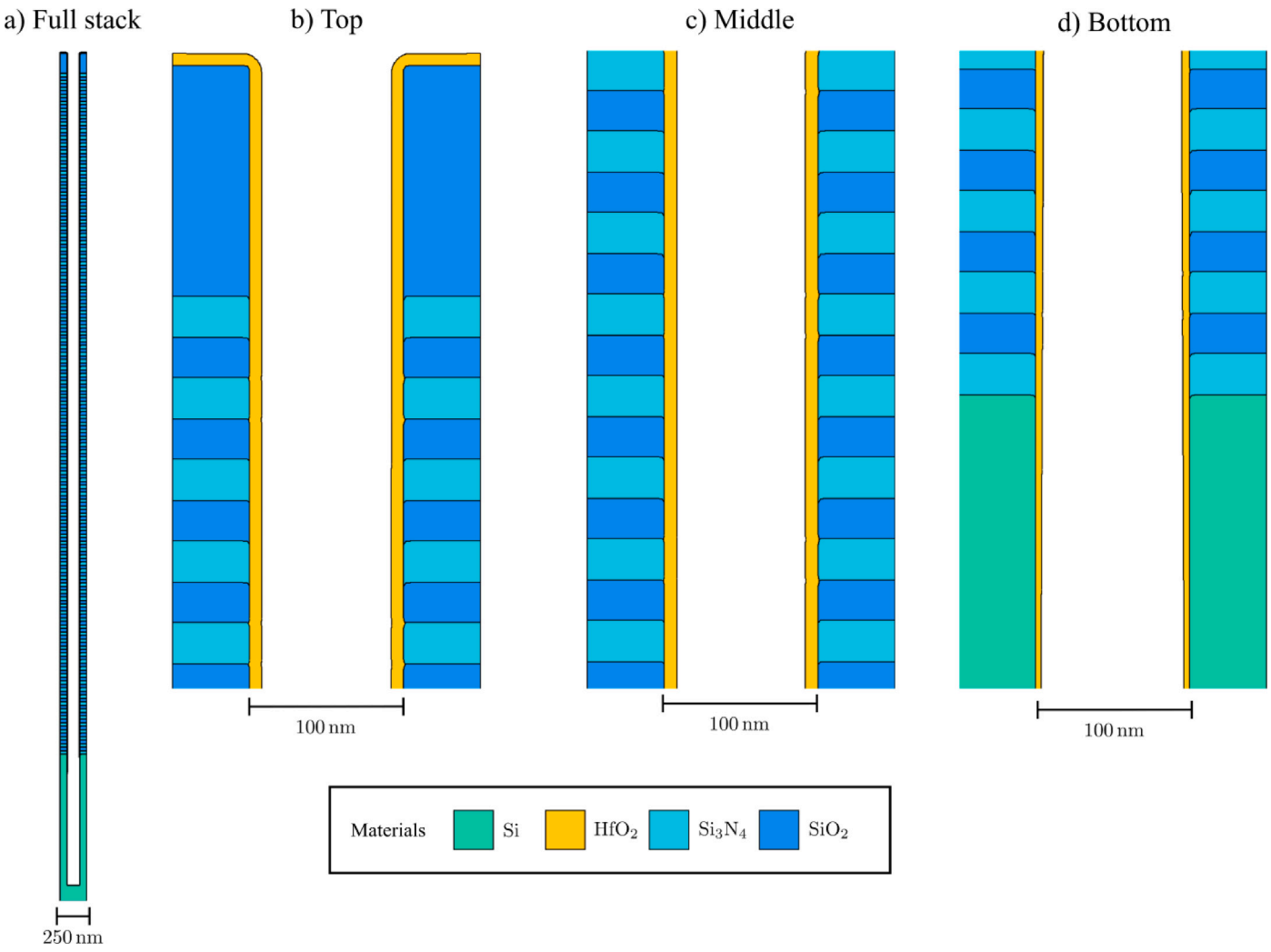

Fig. 9. Cross-section of simulated thermal ALP of HfO_2 inside 3D NAND-like test structure [9] showing different film thickness at three different regions of the full stack (top, middle, and bottom).

transport and reversible first-order Langmuir kinetics, drawing from various established modeling approaches. By focusing on the evaporation flux, our model yields an accurate fit to experimental data and provides valuable insights into the saturation behavior of self-limiting processes. We use the Bosanquet formula to approximate diffusivity, allowing to account for processing conditions with lower Knudsen numbers. Finally, we propose an efficient method of integrating our model with a level-set topography simulator by bundling multiple ALD cycles into a single artificial time unit.

To calibrate our model, we first manually extract reported thickness profiles from a prototypical atomic layer deposition (ALD) process which involves the use of H_2O and TMA to deposit Al_2O_3. Our investigation focuses on the effect of temperature on H_2O-limited profiles, revealing that the evaporation flux has a significant impact at lower temperatures. We extract an activation energy of 0.178 eV, which is consistent with recent experimental studies. By further applying our model to multiple independent experiments in the TMA-limited regime, we confirm that the parameters are highly dependent on the reactor condition, particularly its temperature.

Finally, we apply the same modeling sequence used to generate the Al_2O_3 ALD model to study the ALD and subsequent ALE of HfO_2 in HAR 3D NAND holes. We obtain qualitatively similar results to those measured and reported in literature. The implementation of this model in the commercial Victory Process simulation tool allows for its integration in a complete fabrication sequence. This allows for a further study on the effects of incomplete conformality on device and circuit performance within an integrated DTCO flow.

Declaration of competing interest

The authors declare that they have no known competing financial interests or personal relationships that could have appeared to influence the work reported in this paper.

Data availability

Data will be made available on request.

Acknowledgments

The financial support by the Austrian Federal Ministry of Labour and Economy, the National Foundation for Research, Technology and Development and the Christian Doppler Research Association, Austria is gratefully acknowledged. The authors acknowledge TU Wien Bibliothek, Austria for financial support through its Open Access Funding Program.

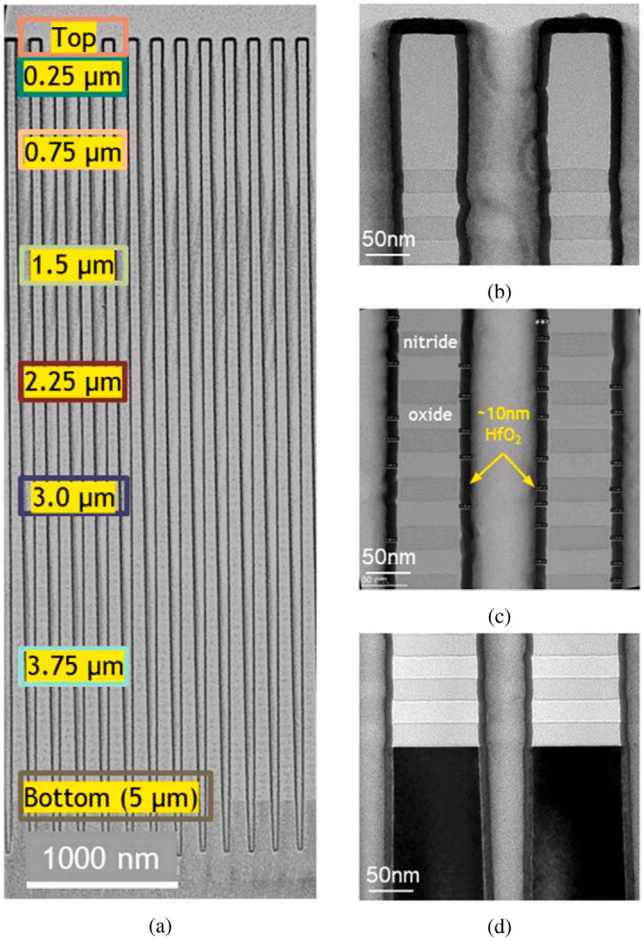

Fig. 10. (a) Cross section of a full 96-pair SiO_2/SiN stack after HfO_2 deposition with post-ALE measurement locations. (b) Close-up of the structure at the top of stack, (c) middle, and (d) bottom. (Reprinted with permission from Fischer et al. *J. Vac. Sci. Technol. A* 40, 022603 (2022) [9]. © 2022, American Vacuum Society).

References

[1] Aguinsky LF, Rodrigues F, Reiter T, Klemenschits X, Filipovic L, Hössinger A, Weinbub J. Modeling incomplete conformality during atomic layer deposition in high aspect ratio structures. Solid State Electron 2023;201:108584–1–108584–6. http://dx.doi.org/10.1016/j.sse.2022.108584.

[2] Lill T. Atomic layer processing. John Wiley & Sons; 2021, http://dx.doi.org/10.1002/9783527824199.

[3] George SM. Atomic layer deposition: An overview. Chem Rev 2010;110(1):111–31. http://dx.doi.org/10.1021/cr900056b.

[4] Fischer A, Routzahn A, George SM, Lill T. Thermal atomic layer etching: A review. J Vac Sci Technol A 2021;39(3):030801–1–030801–17. http://dx.doi.org/10.1116/6.0000894.

[5] Cremers V, Puurunen RL, Dendooven J. Conformality in atomic layer deposition: Current status overview of analysis and modelling. Appl Phys Rev 2019;6(2):021302–1–021302–43. http://dx.doi.org/10.1063/1.5060967.

[6] van Dal M, Vellianitis G, Doornbos G, Duriez B, Holland M, Vasen T, Afzalian A, Chen E, Su S, Chen T, et al. Ge CMOS gate stack and contact development for vertically stacked lateral nanowire FETs. In: Proceedings of the IEEE International electron devices meeting (IEDM). 2018, p. 492–5. http://dx.doi.org/10.1109/IEDM.2018.8614577.

[7] Knoops H, Potts S, Bol A, Kessels W. 27 - Atomic layer deposition. In: Kuech TF, editor. Handbook of crystal growth. 2nd ed.. North-Holland; 2015, p. 1101–34. http://dx.doi.org/10.1016/B978-0-444-63304-0.00027-5.

[8] Jakschik S, Schroeder U, Hecht T, Dollinger G, Bergmaier A, Bartha J. Physical properties of ALD-Al_2O_3 in a DRAM-capacitor equivalent structure comparing interfaces and oxygen precursors. Mater Sci Eng B 2004;107(3):251–4. http://dx.doi.org/10.1016/j.mseb.2003.09.044.

[9] Fischer A, Routzahn A, Gasvoda RJ, Sims J, Lill T. Control of etch profiles in high aspect ratio holes via precise reactant dosing in thermal atomic layer etching. J Vac Sci Technol A 2022;40(2):022603–1–022603–8. http://dx.doi.org/10.1116/6.0001691.

[10] Puurunen RL. Surface chemistry of atomic layer deposition: A case study for the trimethylaluminum/water process. J Appl Phys 2005;97(12):121301–1–121301–52. http://dx.doi.org/10.1063/1.1940727.

[11] Gao F, Arpiainen S, Puurunen RL. Microscopic silicon-based lateral high-aspect-ratio structures for thin film conformality analysis. J Vac Sci Technol A 2015;33(1):010601–1–010601–5. http://dx.doi.org/10.1116/1.4903941.

[12] Hu X. Multiscale simulation of metallic copper and copper oxide atomic layer deposition from cu beta-diketonates (Ph.D. thesis), Technische Universität Chemnitz; 2018, URL https://d-nb.info/121482045X/34.

[13] Ishikawa K, Karahashi K, Ishijima T, Cho SI, Elliott S, Hausmann D, et al. Progress in nanoscale dry processes for fabrication of high-aspect-ratio features: How can we control critical dimension uniformity at the bottom? Japan J Appl Phys 2018;57(6S2):06JA01–1–06JA01–18. http://dx.doi.org/10.7567/JJAP.57.06JA01.

[14] Werbrouck A, Shirazi M, Mattelaer F, Elliott SD, Dendooven J, Detavernier C. A secondary reaction pathway for the alumina atomic layer deposition process with trimethylaluminum and water, revealed by full-range, time-resolved in situ mass spectrometry. J Phys Chem C 2020;124(48):26443–54. http://dx.doi.org/10.1021/acs.jpcc.0c07602.

[15] Gobbert MK, Prasad V, Cale TS. Predictive modeling of atomic layer deposition on the feature scale. Thin Solid Films 2002;410(1–2):129–41. http://dx.doi.org/10.1016/S0040-6090(02)00236-5.

[16] Gordon RG, Hausmann D, Kim E, Shepard J. A kinetic model for step coverage by atomic layer deposition in narrow holes or trenches. Chem Vapor Depos 2003;9(2):73–8. http://dx.doi.org/10.1002/cvde.200390005.

[17] Yanguas-Gil A, Elam JW. Self-limited reaction-diffusion in nanostructured substrates: Surface coverage dynamics and analytic approximations to ALD saturation times. Chem Vapor Depos 2012;18(1–3):46–52. http://dx.doi.org/10.1002/cvde.201106938.

[18] Ylilammi M, Ylivaara OM, Puurunen RL. Modeling growth kinetics of thin films made by atomic layer deposition in lateral high-aspect-ratio structures. J Appl Phys 2018;123(20):205301–1–205301–8. http://dx.doi.org/10.1063/1.5028178.

[19] Szmyt W, Guerra-Nuñez C, Huber L, Dransfeld C, Utke I. Atomic layer deposition on porous substrates: From general formulation to fibrous substrates and scaling laws. Chem Mater 2021;34(1):203–16. http://dx.doi.org/10.1021/acs.chemmater.1c03164.

[20] Schwille MC, Schössler T, Schön F, Oettel M, Bartha JW. Temperature dependence of the sticking coefficients of bis-diethyl aminosilane and trimethylaluminum in atomic layer deposition. J Vac Sci Technol A 2017;35(1):01B119. http://dx.doi.org/10.1116/1.4971197.

[21] Poodt P, Mameli A, Schulpen J, Kessels W, Roozeboom F. Effect of reactor pressure on the conformal coating inside porous substrates by atomic layer deposition. J Vac Sci Technol A 2017;35(2):021502–1–021502–9. http://dx.doi.org/10.1116/1.4973350.

[22] Arts K, Vandalon V, Puurunen RL, Utriainen M, Gao F, Kessels WM, Knoops HC. Sticking probabilities of H_2O and $Al(CH_3)_3$ during atomic layer deposition of Al_2O_3 extracted from their impact on film conformality. J Vac Sci Technol A 2019;37(3):030908–1–030908–5. http://dx.doi.org/10.1116/1.5093620.

[23] Klemenschits X, Selberherr S, Filipovic L. Combined process simulation and simulation of an SRAM cell of the 5nm technology node. In: Proceedings of the international conference on simulation of semiconductor processes and devices (SISPaD). 2021, p. 23–7. http://dx.doi.org/10.1109/SISPAD54002.2021.9592605.

[24] Filipovic L. Modeling and simulation of atomic layer deposition. In: Proceedings of the international conference on simulation of semiconductor processes and devices (SISPaD). IEEE; 2019, p. 323–6. http://dx.doi.org/10.1109/SISPAD.2019.8870462.

[25] Yim J, Verkama E, Velasco JA, Arts K, Puurunen RL. Conformality of atomic layer deposition in microchannels: Impact of process parameters on the simulated thickness profile. Phys Chem Chem Phys 2022;24(15):8645–60. http://dx.doi.org/10.1039/d1cp04758b.

[26] Pollard W, Present RD. On gaseous self-diffusion in long capillary tubes. Phys Rev 1948;73(7):762–74. http://dx.doi.org/10.1103/PhysRev.73.762.

[27] Sethian JA. Level set methods and fast marching methods. 2nd ed.. Cambridge University Press; 1999.

[28] Klemenschits X, Selberherr S, Filipovic L. Modeling of gate stack patterning for advanced technology nodes: A review. Micromachines 2018;9(12):631–1–631–31. http://dx.doi.org/10.3390/mi9120631.

[29] ViennaLS. 2023, Available online: https://github.com/ViennaTools/ViennaLS (accessed 07 February 2023).

[30] Silvaco. Victory process. 2023, Available online: https://silvaco.com/tcad/victory-process-3d/ (accessed 07 February 2023).

[31] Elliott SD, Dey G, Maimaiti Y, Ablat H, Filatova EA, Fomengia GN. Modeling mechanism and growth reactions for new nanofabrication processes by atomic layer deposition. Adv Mater 2015;28(27):5367–80. http://dx.doi.org/10.1002/adma.201504043.

[32] Dkhissi A, Estève A, Mastail C, Olivier S, Mazaleyrat G, Jeloaica L, Rouhani MD. Multiscale modeling of the atomic layer deposition of HfO_2 thin film grown on silicon: How to deal with a kinetic Monte Carlo procedure. J Chem Theory Comput 2008;4(11):1915–27. http://dx.doi.org/10.1021/ct8001249.

[33] Adomaitis RA. Development of a multiscale model for an atomic layer deposition process. J Cryst Growth 2010;312(8):1449–52. http://dx.doi.org/10.1016/j.jcrysgro.2009.12.041.

[34] Heyman A, Musgrave CB. A quantum chemical study of the atomic layer deposition of Al_2O_3 using $AlCl_3$ and H_2O as precursors. J Phys Chem B 2004;108(18):5718–25. http://dx.doi.org/10.1021/jp049762x.

[35] Pan D, Jen T-C, Yuan C. Effects of gap size, temperature and pumping pressure on the fluid dynamics and chemical kinetics of in-line spatial atomic layer deposition of Al_2O_3. Int J Heat Mass Transfer 2016;96:189–98. http://dx.doi.org/10.1016/j.ijheatmasstransfer.2016.01.034.

[36] Keuter T, Menzler NH, Mauer G, Vondahlen F, Vaßen R, Buchkremer HP. Modeling precursor diffusion and reaction of atomic layer deposition in porous structures. J Vac Sci Technol A 2015;33(1):01A104–1–01A104–7. http://dx.doi.org/10.1116/1.4892385.

[37] Yanguas-Gil A, Libera JA, Elam JW. Reactor scale simulations of ALD and ALE: Ideal and non-ideal self-limited processes in a cylindrical and a 300 mm wafer cross-flow reactor. J Vac Sci Technol A 2021;39(6):062404–1–062404–15. http://dx.doi.org/10.1116/6.0001212.

[38] Fang W-Z, Tang Y-Q, Ban C, Kang Q, Qiao R, Tao W-Q. Atomic layer deposition in porous electrodes: A pore-scale modeling study. Chem Eng J 2019;378:122099–1–122099–13. http://dx.doi.org/10.1016/j.cej.2019.122099.

[39] Yanguas-Gil A. Growth and transport in nanostructured materials: Reactive transport in PVD, CVD, and ALD. Springer; 2016.

[40] Chapman S, Cowling TG. The mathematical theory of non-uniform gases. 3rd ed.. Cambridge University Press; 1991.

[41] Knudsen M. Eine revision der gleichgewichtsbedingung der gase. Thermische molekularströmung. Ann Phys 1909;336:205–29. http://dx.doi.org/10.1002/ANDP.19093360110.

[42] Knoops H, Langereis E, Van De Sanden M, Kessels W. Conformality of plasma-assisted ALD: physical processes and modeling. J Electrochem Soc 2010;157(12):G241–9. http://dx.doi.org/10.1149/1.3491381.

[43] ViennaPS. 2023, Available online: https://github.com/ViennaTools/ViennaPS (accessed 07 February 2023).

[44] Osher S, Sethian JA. Fronts propagating with curvature-dependent speed: Algorithms based on Hamilton-Jacobi formulations. J Comput Phys 1988;79(1):12–49. http://dx.doi.org/10.1016/0021-9991(88)90002-2.

[45] Osher S, Shu C-W. High-order esentially nonoscillatory schemes for Hamilton-Jacobi equations. SIAM J Numer Anal 1991;28(4):907–22. http://dx.doi.org/10.1137/0728049.

[46] Quell M, Diamantopoulos G, Hössinger A, Weinbub J. Shared-memory block-based fast marching method for hierarchical meshes. J Comput Appl Math 2021;392:113488–1–113488–15. http://dx.doi.org/10.1016/j.cam.2021.113488.

[47] Quell M, Suvorov V, Hossinger A, Weinbub J. Parallel velocity extension for level-set-based material flow on hierarchical meshes in process TCAD. IEEE Trans Electron Dev 2021;68(11):5430–7. http://dx.doi.org/10.1109/TED.2021.3087451.

[48] Gusev E, Cabral C, Copel M, D'Emic C, Gribelyuk M. Ultrathin HfO_2 films grown on silicon by atomic layer deposition for advanced gate dielectrics applications. Microelectron Eng 2003;69(2–4):145–51. http://dx.doi.org/10.1016/s0167-9317(03)00291-0.

[49] Murdzek JA, George SM. Effect of crystallinity on thermal atomic layer etching of hafnium oxide, zirconium oxide, and hafnium zirconium oxide. J Vac Sci Technol A 2020;38(2):022608–1–022608–8. http://dx.doi.org/10.1116/1.5135317.

[50] Fischer A, Mui D, Routzahn A, Gasvoda R, Sims J, Lill T. Surface reaction modelling of thermal atomic layer etching on blanket hafnium oxide and its application on high aspect ratio structures. J Vac Sci Technol A 2023;41(1):012601–1–012601–10. http://dx.doi.org/10.1116/6.0002244.

[51] Yim J, Ylivaara OM, Ylilammi M, Korpelainen V, Haimi E, Verkama E, et al. Saturation profile based conformality analysis for atomic layer deposition: Aluminum oxide in lateral high-aspect-ratio channels. Phys Chem Chem Phys 2020;22(40):23107–20. http://dx.doi.org/10.1039/d0cp03358h.